



Novel Quantitative Techniques for Assessing Regional and Global Function and Structure Based on Modern Imaging Modalities: Implications for Normal Variation, Aging and Diseased States

Sandip Basu, MD,* Habib Zaidi, PhD,[†] Mohamed Houseni, MD,* Gonca Bural, MD,* Jay Udupa, PhD,* Paul Acton, PhD,[‡] Drew A. Torigian, MD, MA,* and Abass Alavi, MD*

In this review, we describe the current approaches used for quantitative assessment of regional and global function with positron emission tomography (PET) imaging (combined with structural imaging modalities) with emphasis on both research and clinical applications of this powerful approach. We particularly refer to the impact of such measurements in assessing physiological processes such as aging and measuring response to treatment in serious disorders such as cancer. Although a multitude of methods has been described in literature, the optimal approaches that are both accurate and practical in clinical settings need to be defined and refined. Standardized uptake value (SUV) continues to be the most widely used index in the current practice. Calculating SUV at a single time point and assigning standard regions of interest are inadequate and suboptimal for the purposes adopted by the medical community. The concepts of partial volume correction for measured values in small lesions, dual-time point and delayed PET imaging, and global metabolic activity for assessment of various stages of disease may overcome deficiencies that are associated with the current quantitative (ie, SUV) techniques. Serious consideration of these concepts will enhance the role and reliability of these quantitative techniques, and therefore compliment the World Health Organization or the Response Evaluation Criteria in Solid Tumors (RECIST) criteria for managing patients with cancer and other disorders, including physiological states such as aging and serious diseases such as atherosclerosis and neurological diseases. We also introduce the concepts that allow for segmentation of various structural components of organs like the brain for accurate measurement of functional parameters. We also describe complicated kinetic modeling and methodologies that have been used frequently for assessing metabolic and pharmacological parameters in the brain and other organs. Simplified quantitative techniques based on these concepts are described, but should be validated against the kinetic models to test their role as practical tools.

Semin Nucl Med 37:223-239 © 2007 Elsevier Inc. All rights reserved.

¹⁸F-fluorodeoxyglucose (FDG) positron emission tomography (PET) was introduced as a quantitative technique for calculating absolute metabolic rate of glucose in

terms of mg/100 g/min by using complicated mathematical schemes.^{1,2} This technique requires the insertion of an arterial line and procurement of multiple blood samples, several previously determined constants (rate and lumped constants), and a complex operational equation for calculating metabolic rates for glucose. Obviously, this approach can be used in a limited fashion, mostly for research purposes. In addition, the assumptions that are made for calculating the aforementioned parameters are applicable only to normal physiological states and may not be valid in disease conditions. With the widespread utility of PET in both research and clinical domains, efforts have been made to simplify quantitative techniques that are reasonably accurate but sim-

*Department of Radiology, University of Pennsylvania School of Medicine, Philadelphia, PA.

[†]Division of Nuclear Medicine, Geneva University Hospital, Geneva, Switzerland.

[‡]Molecular Imaging, Johnson & Johnson Pharmaceutical R&D, Spring House, PA. Address reprint requests to Abass Alavi, MD, Department of Radiology, Division of Nuclear Medicine, Hospital of the University of Pennsylvania, 3400 Spruce Street, 1 Donner Building, Philadelphia, PA 19104-4283. E-mail: Abass.Alavi@uphs.upenn.edu

ple enough to be used in the day-to-day application of this modality as a practical tool. In this article, we describe the existing and evolving new approaches that may allow accurate assessment of global and regional function and structure by using modern tomographic imaging modalities.

On the basis of the experience gained during the past 2 decades, PET imaging is probably the most optimal noninvasive modality for assessing the regional and global “metabolic picture” of an organ or diseased sites anywhere in the entire body. Visual assessment of the images provided by PET gives a relative and subjective impression regarding the overall landscape of function at the sites examined. Therefore, quantitative analysis has the potential to complement visual image assessment and minimize interobserver variability that is commonly encountered with qualitative techniques.³ Among various functional imaging techniques, PET is considered the most powerful modality for providing an accurate, reliable, and reproducible estimate of various physiological and metabolic parameters. Obviously, such measurements are invaluable both in conducting research and in the day-to-day practice of medicine. For the purposes of this scientific communication, we have intentionally selected issues that relate to quantitative measurement of regional and global glucose metabolism with FDG as a model that can be adopted for other PET procedures.

The various methods of data analysis schemes have been broadly categorized into 3 groups: (1) qualitative analysis, ie, visual assessment; (2) semiquantitative analysis, ie, standardized uptake value (SUV) and lesion-to-background ratio (L:B ratio); and (3) absolute quantitative analysis using nonlinear regression (NLR), Patlak graphical analysis and derived methods, and simplified quantitative methods. Among these analysis schemes, the visual assessment, SUV, L:B ratio, and simplified quantitative methods require minimal effort and are relatively straightforward, whereas absolute quantitative measurements that are based on kinetic modeling can only be generated by dynamic imaging and blood sampling and are therefore not practical in most settings. Because L:B ratios infrequently are used for either research or clinical purposes, we have decided not to discuss this type of measurement in this review.

Qualitative Visual Assessment Versus Quantitation With FDG-PET

Visual assessment continues to play a pivotal role in the interpretation of PET studies. This type of interpretation is based on a contrast between the sites of uptake of radiotracer either as the result of a normal physiological process or as a result of a pathological state compared with the surrounding background. This type of assessment is particularly applicable to FDG-PET imaging in identifying regional glycolysis. With this technique, “metabolic contrast” reflects the concentration of glucose transporter expression in the cell surface, hexokinase activity, and the level of glucose-6-phosphatase in the cell. Despite its simplicity, qualitative interpretation

suffers from several shortcomings, which include defining and using a threshold for assessment of the presence and degree of tracer concentration among other factors. In addition, both inter- and intraobserver reliability of qualitative measurements is poor for both diagnostic and therapeutic trials. Hence, visual assessment, despite its critical role in the daily practice of medicine, is unsuitable for research applications in which objective quantitative measures are desirable and of utmost importance for optimal results.

Quantitative Metabolic Rate Assessment and Kinetic Modeling

Quantitative kinetic analysis yields absolute rates of FDG metabolism and has the potential to measure individual rate constants, thereby providing insight into various components of glucose metabolism such as transport and phosphorylation. Advantages of this approach include availability of dynamic data and low dependency on imaging time. However, the major reason that precludes the use of full kinetic modeling in the clinical scenario is the complex and time consuming study procedure that includes a dynamic scanning protocol and requirement for arterial blood sampling or dynamic imaging of a blood-pool structure to obtain a precise input function.⁴

Tracer kinetic, or compartmental, modeling provides the link between activity levels measured in the functional scan and physiological parameters associated with the metabolism of glucose by tumors, organs, or tissues. This modeling describes the behavior of FDG in cells mathematically, with a certain assumed number of compartments, each of which represents a distinct physical and/or biochemical stage in the behavior of the tracer. Such models were developed to describe the kinetics of the glucose analogs [¹⁴C]-deoxyglucose and FDG in the pioneering work on tracer kinetic modeling.^{1,2,5-7} FDG is transported from the blood pool across the cell membrane by glucose transporters, where it is phosphorylated by the enzyme hexokinase. FDG competes with glucose in the reaction with hexokinase, in which glucose is phosphorylated to form glucose-6-phosphate. Unlike glucose-6-phosphate, phosphorylated FDG does not undergo further metabolism and is trapped in the cells. Therefore, cellular FDG uptake reflects the overall rate of membrane transport and the availability of hexokinase. Dephosphorylation of FDG-6-phosphate is slow and generally is ignored, although more accurate kinetic modeling, which includes this reverse process, can lead to better results.

The extraction of quantitative values from dynamic PET imaging data requires the fitting of the data to a mathematical model that describes the uptake and retention of the tracer in tissue. The dynamic behavior of FDG in vivo is assumed to follow a standard 3-compartment kinetic model (Fig. 1), with w tissue compartments and a single arterial input function. Compartment 1 (C_1) represents the arterial concentration of free FDG in plasma. The first tissue compartment (C_2) represents an extravascular pool of tracer in the tissue that is

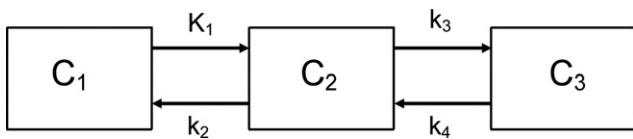


Figure 1 Three-compartment kinetic model of FDG behavior. C_1 is concentration of unmetabolized activity in arterial plasma, C_2 is concentration of free tracer in tissue, and C_3 is concentration of tracer after phosphorylation.

available for phosphorylation, and the final compartment (C_3) is the concentration of FDG that has undergone phosphorylation by hexokinase.

Dynamic imaging data are combined with rapid arterial blood sampling to provide time–activity curves for the specific tumor, organ, or tissue under study. These curves can be fit, generally using nonlinear least squares approximations, to obtain the rate constants $K_1 - k_3$ (k_4 is small and generally ignored). The glucose metabolic rate (MR_{glu}) is calculated by the following equation:

$$\text{MR}_{\text{glu}} = \frac{C_p}{\text{LC}} \times \frac{K_1 \cdot k_3}{k_2 + k_3} = \frac{C_p}{\text{LC}} \times K_i \quad (1)$$

where C_p = plasma glucose concentration, K_1 , k_2 = rate constants for forward and reverse transport of FDG, respectively, k_3 = rate of phosphorylation of FDG, K_i = net rate of influx of FDG, and LC = lumped constant relating FDG kinetics to that of glucose. Errors on MR_{glu}, or on the macroparameter K_i , derive from the variance and covariance of the rate constants extracted from the fitting procedure, which depend strongly on the noise in the imaging data. Separate from these statistical errors are potential biases introduced from a number of sources, including partial volume effects, inaccurate assumptions underlying the model (such as a 0 value for k_4), and the contribution from blood pool activity in the imaging data. Despite these systematic errors, full compartmental kinetic modeling remains the gold standard against which all other techniques, particularly simplified models, are judged.

A number of methods have been proposed, and a significant amount of research has gone into defining the specific rate constants, lumped constant, and other parameters of FDG quantitation. Although originally described in brain imaging,^{8,9} these were extrapolated into tumor imaging as well. The methods described are nonlinear regression (NLR), Patlak graphical analysis, and Patlak derived methods.⁴ These methods (except for the simplified quantitative techniques) all involve dynamic quantitation requiring acquisition of imaging data over 1 h with blood samples drawn at concurrently timed intervals. The regions of interest generated on the reconstructed images and the analysis of radioactivity in the blood at specific time-points enable one to generate time–activity curves for both blood and tissue. The resultant FDG metabolic rate reflects the rate of uptake of FDG into the tissue. Each method has its own pros and cons. However, in general, as stated earlier, they have been used infrequently in clinical practice because of the complexity of such ap-

proaches. The other important factor in oncological imaging is that the patient may have numerous lesions, including both the primary tumor and metastatic lesions, throughout the body. However, the field of view of the study in dynamic imaging methods like NLR or Patlak–Gjedde analysis is limited to 1 bed position. Hence, lesions in the specific bed position can be assessed, but additional scans are required to assess the other lesions. We shall briefly discuss the principles of 2 main quantitative approaches: NLR analysis with a 2-tissue compartment model and simplified tracer kinetic approaches, such as Patlak–Gjedde analysis.

Nonlinear Regression Analysis

In this method, the net rate of FDG influx (K_i) can be calculated from a dynamic PET study and from a standard 2-tissue compartment model, arterial input function, and nonlinear regression analysis.^{1,2,5-7} This method, in addition to being quantitative, is independent of uptake time and provides insight into other rate constants. The usual disadvantages of a dynamic study make its implementation complex.

Patlak–Gjedde Graphical Analysis

This method originally was described by Patlak⁹ for a tracer that is irreversibly trapped in the tissue. With this technique, the regional concentration at time t after injection can be obtained by the following equation:

$$c(t) = \lambda \cdot c_p(t) + K_i \int_0^T c_p(t) dt \quad (2)$$

where $c(t)$ = activity in the tissue as measured by the PET scanner at time t ; $c_p(t)$ = concentration of FDG in the plasma; λ = partition coefficient of FDG; K_i = net rate of FDG influx into the tissue; and T = duration of the PET scan. This method is more robust and offers a number of advantages over NLR analysis, including a simplified scanning protocol, absence of noise amplification, the possibility for generating parametric images, and so on. However, the typical disadvantages of dynamic scanning remain as an obstacle to its routine use. Also, the method is based on the assumption that dephosphorylation (k_4) is negligible and, compared with NLR analysis, individual rate constants like K_1 and k_3 cannot be obtained.

Standardized Uptake Value (SUV): New Concepts

Currently, SUV is the most commonly used semiquantitative parameter in clinical PET studies across the world. Several aliases such as the differential absorption ratio (DAR), differential uptake ratio (DUR), or standardized uptake ratio (SUR) have appeared from time to time in the literature as well. SUV provides a semiquantitative value and is defined as the tissue concentration of tracer, as measured by PET, divided by the

Table 1 Factors Influencing SUV Determination for FDG at Intended Regions of Interest, Their Undesirable Effects, and Associated Required Corrective Measures

Factor	Effects	Corrective Measures
Patient-related factors		
Body size and habitus	Overestimation of SUV in heavier subjects with higher fat content	Use of lean body mass (SUV _{LBM}) or body surface area (SUV _{BSA}) as normalization factor
Serum glucose levels	Reduced FDG uptake in target tissues with increasing blood glucose levels	Control of blood glucose before administering FDG and applying correction factor for glucose level
Technical factors		
Duration of uptake period	Increase in SUV with increasing time in malignant lesions after injection	Standardize initiation of image acquisition following administration of FDG
Partial-volume effects	Underestimation of SUV in lesions with diameters that are smaller than 2-3 times the spatial resolution of the scanner	Adopt an optimal partial volume correction factor
Size of the ROI and nonuniformity of tracer distribution in the lesion	Low SUV _{mean} for large ROIs and high random errors in smaller ROIs	Standard size ROIs placed reproducibly in the same location, SUV _{max} preferable to SUV _{mean}
Attenuation correction and reconstruction methods (spatial filter kernel, image resolution, number of iterations)	Underestimation of SUV with highly smooth reconstruction	Standardize acquisition and reconstruction algorithms for optimal comparison among serial imaging sessions

injected dose normalized to patient weight multiplied by a decay factor.¹⁰

In practice, the SUV is calculated by dividing the activity concentration in the region of interest (ROI) drawn around the lesion (MBq/mL) by the injected dose (MBq) divided by the body weight (g):

$$\text{SUV} = \frac{\text{Tissue activity concentration (MBq/mL)}}{\text{Injected dose (MBq)/Body weight (g)}} \times \frac{1}{\text{decay factor of } ^{18}\text{F}} \quad (3)$$

Advantages and Shortcomings of Simple SUV Measurement and Variables Affecting SUV

SUV quantitation is usually an automated procedure that is available with current software supplied with commercial PET scanners. The major advantages of SUV calculation are that it is computationally simple (with no requirement for blood sampling) and requires considerably less scanner time than the dynamic acquisition protocols. Also, the SUV of the tissue has a linear relationship with the rate of glucose metabolism as measured by kinetic modeling. Two studies^{11,12} have investigated this and registered correlation coefficients of 0.91 and 0.84, respectively. This correlation is improved

further when body surface area is used for normalization rather than body weight. Hence, SUV can be diagnostically as discriminating as the measurement of the metabolic rate for glucose. As a result, static imaging with the generation of SUVs for tumors and other diseases has replaced the more cumbersome dynamic procedure in the routine clinical practice.

Many factors (Table 1) can affect the reliability of SUV.¹³ These include (1) time interval between injection and imaging, (2) degree of infiltration of administered FDG dose at the site of injection, (3) residual activity in the syringe, (4) correction for the decay of the injected dose, and (5) partial volume effects caused by limited spatial resolution of the PET instrument.

SUV and Body Habitus

In most programs, the SUV is normalized to patient body weight (SUV_{BW}). Adipose tissue usually has much less metabolic activity than other tissues. Although body weight was originally used for normalization purposes (Eq. 3), later other parameters such as lean body mass (SUV_{LBM}) and body surface area (SUV_{BSA}) were noted to be superior¹⁴⁻¹⁶ compared with using body weight for accurate calculation of SUV. The latter approach reduces the variation of SUV related to the patient body composition and habitus. Zasadny and coworkers¹⁷ studied the relationship between SUVs in normal tissues and body weight in 28 nondiabetic women with newly diagnosed untreated primary breast

cancer with body weights ranging from 45 to 107 kg, and observed a positive correlation between SUV and body weight for liver and spleen metabolic activity. In heavy patients, SUVs for these tissues were up to two times higher than those of the lighter patients. They proposed correction of SUV for lean body mass (SUV_{LBM}), which, according to these investigators, eliminated the weight dependence of the SUV for blood FDG activity and weight dependence in other tissues. The reason for this observation lies in the fact that FDG uptake is relatively lower in fat compared with other tissues. Hence, in heavier patients with a high fraction of total body fat, which has very low amount of FDG uptake, SUV is overestimated in other tissues.

Kim and coworkers¹⁴ studied the potential for normalization of FDG uptake with body surface area (SUV_{BSA}) in 44 patients with cancer with body weights ranging from 45 to 115 kg. They observed a strong positive correlation between SUV_{BW} and body weight but only a weak correlation between SUV_{BSA} and body weight with a near flat regression line. They concluded that SUV_{BW} overestimates FDG uptake in large patients and that SUV_{BSA} was preferable over SUV_{BW} . Subsequently two studies have confirmed this observation, and have concluded that SUV_{BSA} was superior to both SUV_{BW} and SUV_{LBM} . However, the differences between the normalization methods, according to some authors, appear to be small except in very obese patients.¹⁸

SUV and Blood Glucose Level

Serum glucose levels affect SUV measurement significantly, and many reports have demonstrated that SUVs of malignant lesions are substantially lower when FDG-PET is acquired in hyperglycemic states. In addition, hyperinsulinemia results in increased glycolysis in adipose tissue and in muscles, and therefore in low SUV measurements in other tissues. Most PET centers apply a threshold maximum plasma glucose level ranging from 150 to 200 mg/dL for examining patients before proceeding with FDG-PET. Of interest, it has been observed by some authors¹⁹ that the effects of glucose concentration differ between malignant disorders and inflammatory processes. High concentration levels of blood glucose up to 250 mg/dL do not appear to affect the SUV in inflammatory or other benign lesions.

We must point out that SUV measurement at a single time point by assigning a standard ROI is inadequate for most indications used at this time. Therefore, further refinements of this very useful quantitative measurement are essential for optimal utilization in the day to day practice of medicine.

Changes of SUV Over Time and Implications for Differentiating Benign from Malignant Lesions by Dual-Time Point Imaging

Among the various factors described previously, variations in the time interval between tracer injection and image acquisi-

tion (uptake period) substantially influence SUV. In a study by Hamberg and coworkers,²⁰ the equilibrium time in bronchial carcinoma varied from 256 to 340 minutes after injection and decreased after therapy to 123 to 185 minutes after injection. They concluded that the time interval of 45 to 60 minutes lead to a significant underestimation of true SUV because, in most tumors, FDG uptake continues to increase beyond this period and typically does not reach a plateau for several hours. Lodge and coworkers¹⁴ observed in their study of high-grade sarcomas that tumors reached maximal FDG uptake at 4 hours whereas such equilibrium was achieved within 30 min in benign lesions. Hence, SUV measurements among study populations should be compared at the same time point after tracer administration. FDG uptake over extended time periods (over the course of 7-8 hours) also were studied by investigators at the University of Pennsylvania in patients with nonsmall cell lung cancer.²¹ They were able to demonstrate that although tumor sites revealed increased uptake of FDG during the course of 3 to 4 hours, surrounding normal tissues showed declining values with time.

There is an increasing body of literature describing non-specific were accumulation in a wide spectrum of physiological states as well as in several benign pathologies. Although this has led to active research concerning the role of this modality in assessing disorders such as infection and inflammation, there is a growing concern about the specificity of this technique in effective management of patients with cancer where detecting and measuring disease activity is the main focus for FDG-PET imaging. It is now abundantly clear that considerable overlap of SUV exists between active inflammatory processes and malignant lesions and that a threshold value for SUV alone cannot be generally applied to differentiate between the 2. Several approaches have been explored to enhance the specificity of FDG-PET for examining several malignancies of which dual-time point FDG-PET imaging appears to be the most promising.

The recent literature describes the usefulness of dual-time point FDG-PET in this regard, and the technique has been applied to a wide variety of malignancies, including those of the head and neck,²² lung,²³ breast,²⁴⁻²⁶ gallbladder,²⁷ cervix,²⁸ and central nervous system.²⁹ The theoretical basis of this approach stems from the fact that dephosphorylation in tumor cells is either absent or very slow compared with that in normal cells because of their low glucose-6-phosphatase content. This results in a build up of contrast between malignant lesions and the normal tissues with time, which further enhances lesion detectability. Furthermore, this has been successfully exploited in distinguishing malignant from benign lesions, where changes in SUV over time are significantly different between these two distinct pathologic entities.

Hustinx and coworkers²² studied the utility of dual-time point scanning in 21 patients with head and neck cancer who were scanned serially at 2 time points, the first at 70 minutes (range, 47-112) and the second at 98 minutes (range, 77-142) after the intravenous injection of FDG. The mean interval between emission scans was 28 minutes (range, 13-49). SUVs were generated for the cerebellum, tongue, larynx, ma-

lignant lesion, and a matched contralateral site. Tumor SUVs were 4.0 ± 1.6 (mean \pm SD) for the first scan and 4.5 ± 2.2 for the second scan. Corresponding SUVs for the contralateral sites were 1.2 ± 0.5 and 1.1 ± 0.5 for the 2 scans, respectively. Tumor SUVs increased by $12\% \pm 12\%$ as compared with a $5\% \pm 17\%$ decrease for contralateral sites ($P < 0.05$). SUVs for inflammatory lesions (2.0 ± 0.7 and 2.0 ± 0.9), cerebellum (4.2 ± 1.3 and 4.3 ± 1.4), tongue (1.8 ± 0.4 and 1.9 ± 0.5) and larynx (1.5 ± 0.6 and 1.5 ± 0.6) remained constant over time ($+0.6\%$, $+2.8\%$, $+1.4\%$, and -2.4% ; $P < 0.05$ when compared with tumor SUV changes). The ratio of tumor SUV to contralateral SUV increased by $23\% \pm 29\%$ over time whereas this ratio for inflammatory sites increased by only $5\% \pm 15\%$ ($P = 0.07$). They proposed this approach as a useful means for differentiating malignant lesions from inflammation and nonspecific uptake in normal tissues.

Matthies and coworkers²³ adopted this method for the assessment of pulmonary nodules. Thirty-six patients with 38 known or suspected malignant pulmonary nodules underwent PET scanning of the thorax at 2 time points: the first was at 70 minutes (range, 56-110) and the second was at 123 minutes (range, 100-163) after the intravenous administration of FDG. Tumor SUVs at the first and second time points were 3.66 ± 1.95 and 4.43 ± 2.43 , respectively (ie, $20.5\% \pm 8.1\%$ increase between the 2 measurements; $P < 0.01$). Four of 20 malignant tumors had SUVs of <2.5 on the first scan (range, 1.12-1.69). Benign lesions at the first and second time points had SUVs of 1.14 ± 0.64 and 1.11 ± 0.70 , respectively (P value not significant). In this study, single-time point PET scanning with a threshold SUV of 2.5 (at time point 1) had a sensitivity of 80% and a specificity of 94%, while dual-time point scanning with a threshold value of a 10% increase in SUV between the first and second time points provided a sensitivity of 100% and a specificity of 89%.

Recent studies by Kumar and coworkers²⁵ and Mavi and coworkers²⁶ reported high sensitivity, specificity, and accuracy in breast carcinoma with a dual-time point approach. Kumar and coworkers studied 54 breast cancer patients with 57 breast lesions who underwent 2 sequential FDG-PET scans. The average percent change in the SUVs between time point 1 and time point 2 was calculated. All PET study results were correlated with follow-up surgical pathology results. Of the 57 breast lesions, 39 were invasive carcinoma and 18 were postbiopsy inflammation. Among the invasive carcinomas, 33 (85%) showed an increase and 6 (15%) showed either no change or a decrease in SUV over time. The percent change in SUVs in these tumors from time point 1 to time point 2 (mean \pm SD) was $+12.6\% \pm 11.4\%$ ($P = 0.003$). Of the 18 inflammatory lesions, 3 (17%) showed an increase and 15 (83%) showed either no change or a decrease in SUVs. The percent change in SUVs from the time point 1 to the time point 2 (mean \pm SD) was $-10.2\% \pm 16.5\%$ ($P = 0.03$). Of the 57 normal contralateral breasts, 2 (3.5%) showed an increase and 55 (96.5%) showed either no change or a decrease in SUVs. The percent change in SUVs from time point 1 to time point 2 (mean \pm SD) was $-15.8\% \pm 17\%$ ($P = 0.005$).

In the study by Mavi and coworkers,²⁶ 152 patients with newly diagnosed breast cancer underwent 2 sequential PET scans for preoperative staging, and SUV_{max} was measured at both time points. The percent change in SUV_{max} (Δ SUV_{max}%) between time points 1 (SUV_{max1}) and 2 (SUV_{max2}) was calculated. Patients were divided into 2 groups according to histopathology as invasive and noninvasive. Invasive tumors also were divided into 2 groups (>10 mm and 4-10 mm). The tumor-to-contralateral normal breast (background) ratios of SUV_{max} at both time points for these 2 groups were measured, and Δ %SUV_{max} values were calculated. The mean \pm SD of the SUV_{max1}, the SUV_{max2}, and the Δ %SUV_{max} were 3.9 ± 3.7 , 4.3 ± 4.0 , and $8.3\% \pm 11.5\%$ for invasive; 2.0 ± 0.6 , 2.1 ± 0.6 , and $3.4\% \pm 13.0\%$ for noninvasive; and 1.2 ± 0.3 , 1.1 ± 0.2 , and $-10.0\% \pm 10.8\%$ for the contralateral normal breast groups, respectively. When SUV_{max1}, Δ %SUV_{max}, and the tumor-to-background ratios were compared among groups, all results were found to be significant ($P < 0.001$). They concluded that dual-time point imaging is a simple and noninvasive method that may improve the sensitivity and accuracy of FDG-PET in assessing patients with primary breast cancer.

Lesion detectability increased from 83% at 1.5-hour images to 93% at 3-hour images in a study by Boerner and coworkers²⁴ in breast carcinoma. Ma and coworkers²⁸ investigated the usefulness of dual-phase FDG-PET scans in detecting para-aortic lymph node (PALN) metastases from cervical cancer. These data revealed that an additional scan at 3 hours is helpful for detecting PALN, especially for lower PALN metastases. Nishiyama and coworkers²⁷ adopted this method in gallbladder carcinoma and concluded that delayed FDG-PET is more helpful than early FDG-PET for evaluating malignant lesions. Spence and coworkers²⁹ applied this method in supratentorial gliomas coupled with kinetic modeling. The estimated k_4 values for tumors were not significantly different from those of cerebral gray matter (GM) in early imaging but were lower at the delayed times. A report by Zhuang and coworkers³⁰ revealed an increase in SUV on delayed scans in known malignant lesions, whereas the SUVs of benign lung nodules decreased slightly over time, and those of the inflammatory lesions caused by radiation therapy and of lesions of painful lower limb prostheses remained stable over time. The application of this approach to predict the nature of the bone marrow FDG uptake was studied by Houseni and coworkers³¹. They noted that malignant lesions in the bone marrow result in significantly higher levels of FDG uptake over time than those affected by chemotherapeutic agents, whereas there is a substantial decrease in SUV on repeat scans. Hence, they concluded that there is a significant difference in the dynamics of FDG uptake over time in different histopathological states of the bone marrow.

It is important to note that in many of these studies, dual-time point PET improved both the sensitivity and the specificity of PET for various malignancies, including breast cancer, lung cancer, and head and neck cancer. Theoretically this is due to two factors: continued increased uptake in malignant lesions helps to differentiate them with higher specificity, and increased lesion-to-background contrast (resulting

from a combination of FDG washout from surrounding normal tissues and enhanced FDG uptake in malignancy) leads to higher sensitivity of lesion detection. This is notable since in general, there is a trade-off between sensitivity and specificity for most other diagnostic imaging tests, usually indicating that improvement in performance of one of these parameters results in worsened performance in the other.

These data clearly demonstrate that relying solely on absolute measurements with SUV or other parameters may not allow optimal separation of malignant lesions from benign abnormalities. Therefore, change in SUV may prove to be superior for improving both the specificity and the sensitivity of this quantitative technique.

Partial Volume Correction of SUV

The partial volume effect (PVE) is one of the important limiting technical factors for accurate quantitation with PET, mostly related to the scanner resolution. However, physiological and patient motion during data acquisition are also major factors in degrading spatial resolution, thereby also contributing to the PVE. The phenomenon is also applicable to other imaging techniques including SPECT and structural imaging, when objects with less than 2 to 3 times the spatial resolution of the scanner are examined. This effect has been extensively addressed in brain PET studies,³²⁻³⁹ when attempts were made to measure the exact concentration of the tracers such as FDG in the brain. The spatial resolution of PET systems varies among the current models. Typically, the best resolution (as measured by phantoms) achieved by the modern generation of clinical whole-body PET scanners is at best 4 mm. However, in practice the actual spatial resolution of the images reconstructed is substantially less than that specified by laboratory experiments. This limited spatial resolution does not allow for an accurate measurement of the true concentration of the radiotracer in structures and lesions less than 2 to 3 times the spatial resolution of the PET scanner as defined by the full-width at half-maximum of a point spread function.

The contrast between the lesion and the surrounding background decreases as the size of the lesion becomes smaller, and may disappear completely beyond a certain point.⁴⁰ One method to correct for the PVE is to use the lesion size as determined by CT as the basis for the calculation of the correct SUV. Hickeson and coworkers⁴¹ investigated the implications of this effect in the assessment of pulmonary lesions, and noted that there is a significant underestimation of SUV in lesions smaller than 2 cm in size. By correcting the measured value by using lesion size measured from the CT scan (which was assumed to represent the true size of the lesion), improved differentiation between malignant and benign lesions was noted. Avril and coworkers¹⁸ examined the role of a similar approach in breast cancer, and noted that correction of SUV for the PVE and normalization for blood glucose level yielded the highest diagnostic accuracy among several PET quantitative procedures. Lubberink and cowork-

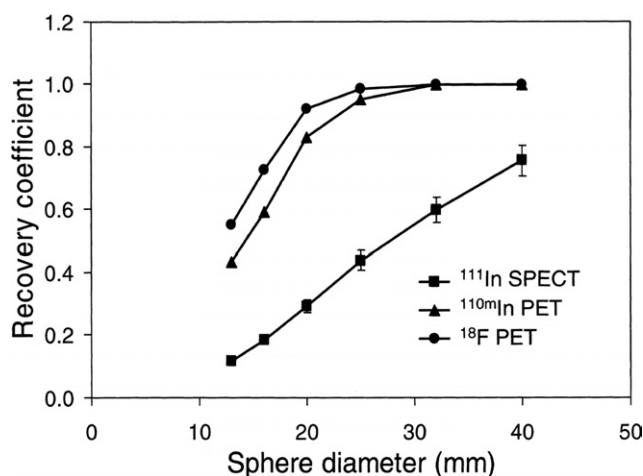


Figure 2 Sphere recovery functions for partial volume correction for ^{110m}In-PET, ¹¹¹In-SPECT, and FDG-PET. (Reprinted with permission of the Society of Nuclear Medicine from Lubberink et al.⁴²)

ers⁴² compared the results of ^{110m}In-DTPA-D-Phe¹-octreotide PET images with those of the ¹¹¹In-DTPA-D-Phe¹-octreotide SPECT scans, and observed that partial volume correction greatly improved detection of small tumors and allowed accurate quantitation of tracer concentration in lesions of various sizes (Fig. 2). The PVE correction is of great importance in the setting of monitoring response to therapeutic intervention, where the reduction in the size of a tumor could result in underestimation of the true concentration of compounds such as FDG in the intended sites.

Applications of Partial Volume Correction in Clinical Scenarios

Applications in Oncology

One method to correct for the resolution effect is to use the lesion size determined on CT or MR imaging as the basis for calculating the SUV. Hickeson and coworkers⁴¹ reported an increase in accuracy from 58% to 89% by using this technique for assessing metabolic activity of lung nodules measuring less than 2 cm when a SUV threshold of 2.5 was adopted to distinguish between benign and malignant lesions (Figs. 3-6). In this study, each lesion's SUV was determined by using 2 different methods. The maximum voxel SUV was determined in a circular ROI with a diameter of 0.8 cm (2 voxels) at the plane with maximal FDG uptake in the lesion. In the second method, the SUV was corrected for underestimation of the true metabolic activity of the entire lesion because of the suboptimal spatial resolution and the PVE. Two ROIs were drawn around the lesion. The smaller of the 2 included all voxels associated with the lesion. In practice, this was drawn at least 0.8 cm outside the 50% uptake level of the maximum activity to include all of the counts resulting from the solitary pulmonary nodule. The second larger ROI surrounded the smaller ROI as well as its surrounding background. Thus, lesion background could be determined from the average uptake outside the smaller ROI and inside the

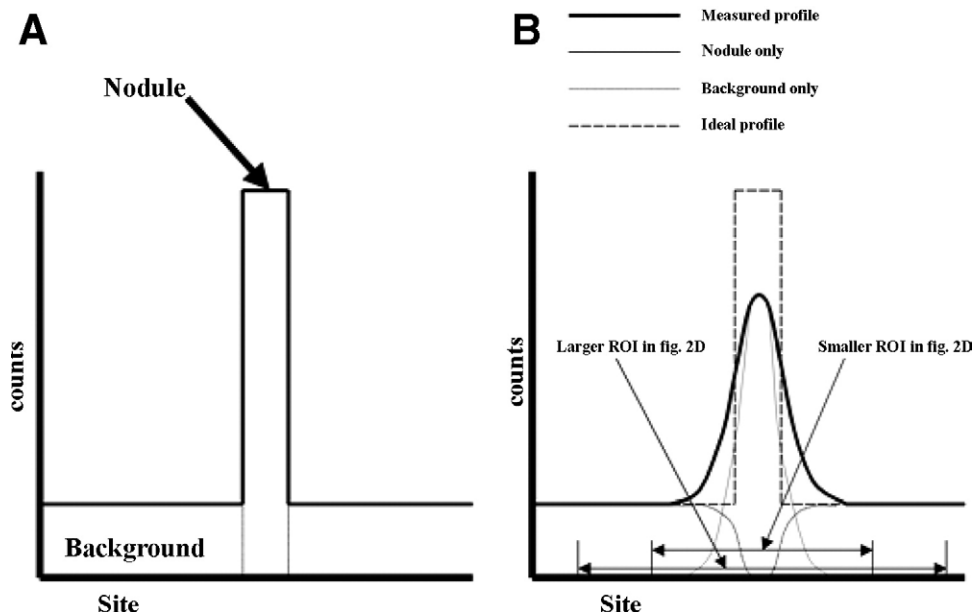


Figure 3 (A) Profile of small lung nodule with uniform FDG uptake using “ideal” PET scanner with perfect spatial resolution; lung itself shows uniformly low FDG activity. (B) Profile of perceived FDG activity with current PET scanner through same nodule in same lung is indicated by thick-lined curve. True distribution of FDG (ideal profile) is indicated by broken line. Thin line indicates profile of perceived FDG activity from lung nodule and thinner line indicates that from uninvolved adjacent lung parenchyma (background). Note that area under profile using “ideal” PET scanner indicated in A is equal to that using current PET scanner indicated in (B). (Reprinted with permission of Springer Science and Business Media from Hickeson et al.⁴¹)

larger ROI. Note that the halfway point between the maximum lesion activity and the surrounding background activity is frequently used as the true size of the lesion. The background uptake was then subtracted from the average uptake in the small ROI. Therefore, the corrected SUV was calculated by including the injected dose, the patient’s weight, and time after injection by using the following formula:

corSUV

$$= \frac{\left(\frac{\text{Region's activity (MBq)} - \text{Background activity (MBq)}}{\text{Lesion's size on CT scan (cm}^3\text{)}} \right)}{\left(\frac{\text{Injected dose (MBq)}}{\text{Body weight (g)}} \right)} \quad (4)$$

Applications in Neurology

Correction for partial volume correction was used by investigators at the University of Pennsylvania in the 1980s when CT and low-resolution PET instruments were used to examine patients with Alzheimer’s disease (AD) and other central nervous system disorders that usually result in cerebral atrophy.³² This technique was later investigated by using modern segmentation methodologies and high-resolution MR imaging.^{43,44} The latter has allowed for accurate measurement of GM and white matter (WM) as well as cerebral spinal fluid (CSF) volumes in the brain.^{45,46}

Kohn and coworkers⁴⁵ described a new computerized system developed to process standard spin-echo magnetic reso-

nance imaging data for estimation of brain parenchyma and cerebrospinal fluid volumes. In phantom experiments, these estimated volumes corresponded closely to the true volumes ($r = 0.998$), with a mean error less than 1.0 cm³ (for phantom volumes ranging from 5 to 35 cm³), with excellent intra- and interobserver reliability. In a clinical validation study with actual brain images of 10 human subjects, the average coefficient of variation among observers for the measurement of absolute brain and CSF volumes was 1.2% and 6.4%, respectively. The intraclass correlation for 3 expert operators was found to be greater than 0.99 in the measurement of brain and ventricular volumes and greater than 0.94 for total CSF volume. The authors concluded that their technique to analyze MR images of the brain performed with acceptable levels of accuracy, and concluded that it can be used to measure brain and CSF volumes for clinical research. This technique, they believed, could be helpful in the correlation of neuroanatomic measurements to behavioral and physiological parameters in neuropsychiatric disorders.

Tanna and coworkers³³ adopted this computerized segmentation technique in a retrospective analysis of digitized T2-weighted MR images of 16 healthy elderly control subjects and 16 patients with AD. They quantified ventricular and extraventricular CSF and studied the effects of aging and AD on brain function as determined by FDG-PET. In both groups, the degree of atrophy as measured by these techniques was used to correct for metabolic rates obtained by PET. Patients with AD had higher total; extraventricular, total ventricular, and third ventricular CSF volumes (49%, 37%, 99%, and 74%, respectively),

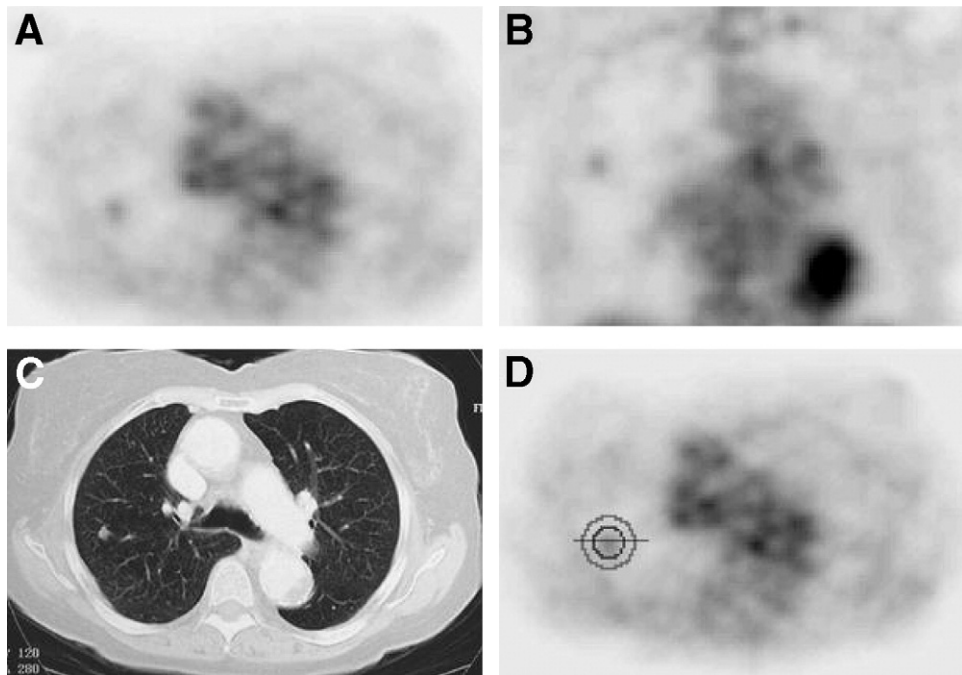


Figure 4 A 72-year-old woman with small cell lung carcinoma is shown. In (A) and (B), axial and coronal images of FDG-PET scan demonstrate focus of mildly increased uptake in right middle lobe. SUV_{max} was 1.39, which is less than threshold for malignancy. (C) Axial chest CT image demonstrates that nodule measures 1.0×0.8 cm.

D, corSUV was obtained by drawing ellipsoid or circular ROI (in black) with diameter of 0.8 cm (2 voxels) larger than that of area of perceived increase in activity at plane of maximal FDG uptake, and drawing another ROI (in gray) with diameter of 0.8 cm larger than first ROI to determine background activity (activity per volume outside smaller ROI and inside larger ROI). corSUV was then obtained by determining activity in first smaller ROI corrected for background activity, dividing by lesion's size on CT and ratio of injected dose to body mass, and correcting for decay of ^{18}F . corSUV of this lesion was 3.54, which exceeds threshold for malignancy. Horizontal line through nodule approximates profile in Figure 4B. (Reprinted with permission of Springer Science and Business Media from Hickeson et al.⁴¹)

and 7% lower brain volumes than the control group. Patients with AD also showed a more marked decline in brain volumes and a greater increase in CSF volumes with advancing age than the control group. The patient group had a 25.0% increase in corrected whole-brain metabolic rates compared with the con-

trol group who had only a 15.8% increase by applying the partial volume correction factors. The use of this technique, they concluded, could provide a basis for further studies of aging and dementia, by calculating the accurate rates of regional metabolism in these settings.

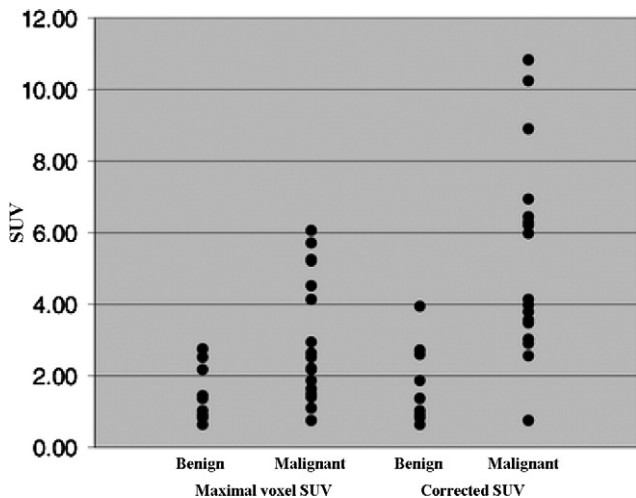


Figure 5 SUVs of benign and malignant lung lesions measuring equal to or less than 2 cm using both methods. (Reprinted with permission of Springer Science and Business Media from Hickeson et al.⁴¹)

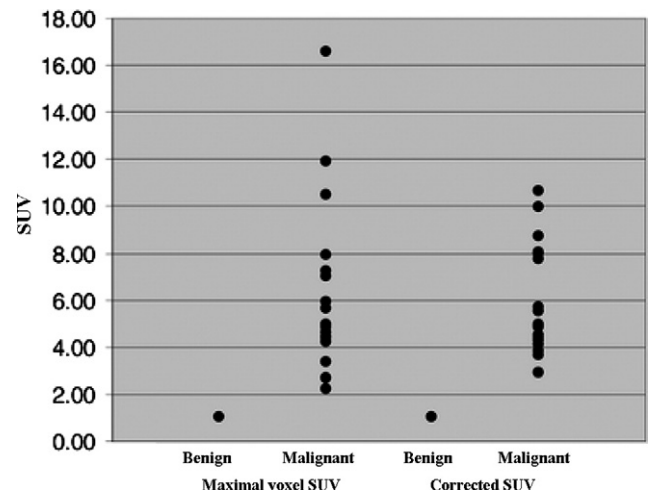


Figure 6 SUVs of benign and malignant lung lesions measuring more than 2 cm using both methods. (Reprinted with permission of Springer Science and Business Media from Hickeson et al.⁴¹)

Bural and coworkers⁴⁷ studied the effects of a novel quantitative MR imaging segmentation scheme that allows for actual SUV (instead of metabolic rates as reported by Tanna and coworkers as referenced previously) calculation of the regional GM, WM, and CSF volumes. This approach resulted in overcoming the difficulties associated with conventional low resolution imaging techniques for measuring actual metabolic activity of the GM. These investigators calculated the volumes of GM, WM, and CSF by using a special segmentation technique on the MR images. This was followed by computation of the mean SUV representing the whole metabolic activity of the brain from the FDG-PET images. They also measured the WM SUV from the upper transaxial slices (centrum semiovale) of the FDG-PET images. The volumes of the GM, WM, and CSF were summed to calculate whole brain volume to enable calculation of global cerebral metabolic activity by multiplying the mean SUV by the total brain volume. Similarly, the whole-brain WM metabolic activity was measured by multiplying the mean SUV for the WM by the WM volume. CSF metabolic activity was considered to be 0. Thus, by subtracting the global WM metabolic activity from that of the whole brain, they were able to measure the global GM metabolic activity alone. Finally, by dividing GM global metabolic activity by GM volume, an accurate SUV for GM alone was determined. The brain volumes ranged between 1100 to 1546 cm³. The mean SUV for total brain was 4.8 to 7. Global cerebral metabolic activity of the brain ranged from 5565 to 9566 SUV-cm³. The mean SUV for WM was 2.8 to 4.1. On the basis of these measurements, they reported that the GM SUV in the sample examined ranged from 8.7 to 11.3.

Advances in Medical Image Segmentation

Image segmentation, the process of identifying objects of interest in the given multidimensional image and delineating their spatial occupation in the image, has been identified as the key problem of medical image analysis, and remains a popular and challenging area of research.⁴⁸ Image segmentation is increasingly used in many clinical and research applications to analyze medical imaging data sets and consists of 2 related tasks: *recognition* and *delineation*. Recognition is the process of roughly determining the object's whereabouts in an image and does not involve the precise specification of the region occupied by the object. It is a high-level act of indicating, for example, on an MR image of the human brain, that "this is the white matter object, this is the gray matter object, this is the cerebrospinal fluid object," etc. Human-assisted recognition can be accomplished, for example, by using the mouse cursor to point at object regions or to specify seed points. Delineation is the process of determining the object's precise spatial extent and composition including gradation. If bone is the object system of interest in an image of the knee, for example, then delineation consists of defining the spatial extent of the femur, tibia, fibula, and patella separately and for each voxel in each object, specifying an objectness value.

Once the objects are defined separately, the bones can be individually visualized, manipulated and analyzed.

Knowledgeable humans usually outperform computer algorithms in the high-level task of recognition. However, carefully designed computer algorithms outperform humans in the precise, accurate, and efficient delineation. Clearly, human delineation that can account for graded object composition (which comes from natural object material heterogeneity, noise, and various artifacts such as partial volume effects) is impossible. Most of the challenges in completely automated segmentation may be attributed to the shortcomings in computerized recognition techniques, and to the lack of delineation techniques that can handle graded composition and the tendency of voxels to hang together in space (as a fuzzy cloud) in the presence of this gradation. In the rest of this section, we will present a brief overview of image segmentation with examples illustrated in the clinical applications considered in this paper.

Emphasis on object recognition is far less in the literature than on delineation. Hence, we shall focus mainly on delineation methods in this review. A large variety of methods are available for delineation. Often, delineation is itself considered to be the total segmentation problem, as such its solutions are considered to be equivalent to solutions to the entire segmentation problem. It is, however, helpful to distinguish between recognition and delineation for understanding, and hopefully solving, the difficulties encountered in segmentation. Approaches to delineation can be broadly classified as boundary-based, region-based, and hybrid. *Boundary-based* methods output an object description in the form of a boundary surface that separates the object from the background. The boundary description may be as a hard set of primitives, ie, points, polygons, surface patches, voxels, etc., or as a fuzzy set of primitives such that each primitive has a grade of "boundariness" associated with it. *Region-based* methods produce an object description in the form of the region occupied by the object. The description may be simple as a (hard) set of voxels, in which case each voxel in the set is considered to contain 100% object material, or as a fuzzy set, in which case membership in each voxel may be any number between 0 and 100%. Previous information about object shape is more easily captured via boundaries than in region description. *Hybrid methods* attempt to combine information about boundaries and regions in seeking a solution to the delineation problem. If we combine the approaches for recognition and delineation, there are 12 possible classes of approaches to segmentation. Much has been written elsewhere about medical image segmentation algorithms, and as such, interested readers are encouraged to consult the detailed and comprehensive reviews and book chapters published on the subject.^{3,49-51}

Within the context of quantitative PET imaging, image segmentation has found numerous clinical and research applications.³ This includes estimation of organ volumes or tumor volumes as well as definition of target treatment volumes in radiation therapy,⁵² extraction of parameters of clinical relevance such as the left ventricular region in nuclear cardiology,⁵³ automated ROI delineation of structures of in-

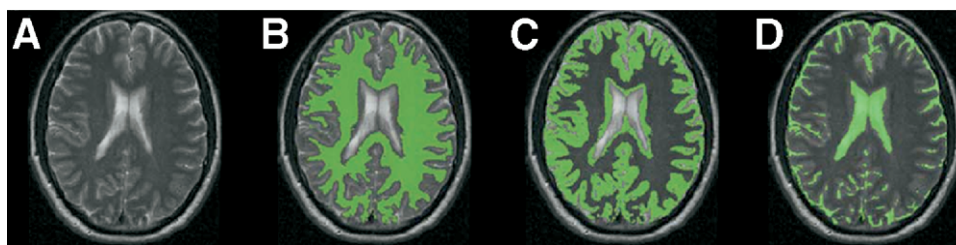


Figure 7 Segmentation technique used to calculate SUV in GM, WM, and CSF. (A) Axial slice of intensity inhomogeneity corrected and intensity standardized T2-weighted image. (B-D) Color overlays on same axial T2-weighted image corresponding to segmented WM, GM, and CSF, respectively. (Images courtesy of Jay Udupa, PhD).

terest in dynamic functional imaging,⁵⁴ generation of functional images to highlight regions of similar temporal behavior (components),⁵⁵ determination of the attenuation map in emission tomography,⁵⁶ anatomically-guided image reconstruction and partial-volume segmentation,³⁷ and construction of voxel-based anthropomorphic phantoms based on high-resolution anatomical images. For the latter, the interested reader is referred to a recent review describing the development of such computational models in connection with Monte Carlo modeling tools in radiological sciences.⁵⁷

One example (Fig. 7) of the application of image segmentation shows a representative slice of a clinical T2-weighted MR image through the brain and the corresponding segmentation results separately showing each tissue class (GM, WM, CSF). MR images were first corrected for inhomogeneity and were subsequently intensity standardized before applying a segmentation method on them. The mean intensity and standard deviation for each of GM, WM, and CSF regions are then estimated from the training data set and are fixed once for all. A fuzzy connectedness framework was utilized for creating a brain intracranial mask, and the fuzzy membership value of each voxel in each brain tissue was estimated, and final segmentation of the brain tissues was simply performed via a maximum likelihood criterion as described by Zhuge and coworkers.⁴⁶

Another example involves segmentation of the lung parenchyma. Historically, segmentation of the lungs on CT scans was a popular research subject given its usefulness in computer-based analysis of thoracic CT images and computer-aided diagnosis. As a consequence, plenty of image segmentation approaches were proposed and many of them found applications in clinical settings. For example, the software system 3DVIEWS⁵⁸ was used to segment the CT image of the lungs to obtain the left and the right lung. The steps were as follows: (1) The *Threshold* operation was used to segment the lung tissue from the rest of the CT image. (2) Subsequently, *Interactive2D* was used to manually remove the areas that were not a part of the lungs or were a part of the airway tree. (3) The mask that was produced covered the lung area only. Using *Interactive2D* once again, the left lung was removed and hence the mask for the right lung was obtained. (4) *Algebra* was used to obtain the left lung by subtracting the right lung mask from the entire lung mask. Figure 8 displays the segmentation results on a chest CT in one subject.

Within the realm of oncological PET imaging, image seg-

mentation is vital for a variety of specific applications for tumor quantitation in staging, assessment of tumor response to therapy, and definition of target volumes in radiation therapy treatment planning.⁵⁹ One such novel automated system for the segmentation of oncological PET data aiming at providing an accurate quantitative analysis tool was recently proposed.⁵² The initial step involves expectation maximization (EM)-based mixture modeling using a k-means clustering procedure, which varies voxel order for initialization. A multiscale Markov model is then used to refine this segmentation by modeling spatial correlations between neighboring image voxels. Anthropomorphic phantom experiments were conducted for quantitative evaluation of the performance of the proposed segmentation algorithm. The comparison of actual tumor volumes to the volumes calculated using different segmentation methodologies including standard k-means, spatial domain Markov Random Field Model (MRFM), and the new multiscale MRFM showed that the latter dramatically reduces the relative error to less than 8% for small lesions (7-mm radii) and less than 3.5% for larger lesions (9-mm radii). The analysis of the resulting segmentations of clinical oncologic PET data seems to confirm that this methodology shows promise and can successfully segment patient lesions. For problematic images (Fig. 9), this technique enables the identification of tumors situated very close to nearby high normal physiological uptake.

To enhance lesion detectability, the use of similarity measures for analysis of dynamic oncological imaging to enhance the contrast between normal tissues and lesions is an appealing approach that needs to be investigated further.⁶⁰ One such technique, proposed originally for cardiac imaging and now being investigated for oncology PET studies, uses the cross- ψ_B -energy operator, a nonlinear similarity measure

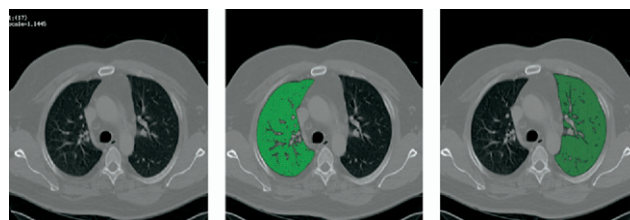


Figure 8 Illustration of lung CT segmentation results. From left to right: original axial CT image, right lung segmentation, and left lung segmentation. (Images courtesy of Jay Udupa, PhD.)



Figure 9 Illustration of automated segmentation procedure for PET. From left to right: original clinical image, resultant segmentation (8 segments) utilizing traditional MRFM, and resultant segmentation using multiscale MRFM. (Adapted with permission from Montgomery et al.⁵²)

which quantifies the interaction between 2 time-signals including their first and second derivatives.⁵⁵ Similarity measure between the time activity curve (TAC) of each pixel and the mean value of the TACs of a reference region of the dynamic image series is calculated, thereby generating images demonstrating temporal changes in radioactive tracer distribution.

As far as partial volume correction is concerned, the accuracy of algorithms depends in part on the degree of accuracy in the segmentation of the anatomical images and the coregistration of anatomical images with the PET data. These effects have been investigated extensively in the literature for both the voxel-based and region-based partial volume correction strategies.^{36,39,61} It was demonstrated that errors in the segmentation procedure have greater impact but are relatively limited to the mis-segmented region.⁶¹ Overall, it appears that the success of the segmentation of the structural information provided by MR images, for instance, has a higher impact on the accuracy of the corrected estimates,³⁹ compared with the influence of image coregistration, although some authors recently suggested that mis-registration errors have the strongest impact on data accuracy and precision.³⁶ Notwithstanding, it was suggested that in the absence of major sources of registration or segmentation errors, recovered activity concentration estimates have been found to be typically within 5% to 10% of true tracer concentration with a standard deviation of a few percent in both phantom and simulation studies.^{34-36,61} An important development that can be exploited for future simultaneous PET/MR imaging technology dedicated for brain research is to combine various MR imaging segmentation methodologies for both partial volume correction and attenuation compensation.⁶²

Concept of Global Metabolic Activity Based on Combined Structure-Function Assessment in Healthy and Diseased States

The concept of global metabolic activity was first introduced by Alavi and coworkers⁶³ in assessment of the brain in patients with AD and in age-matched controls. These investigators were able to demonstrate that by multiplying segmented brain volumes as determined from MR images by the measured mean cerebral metabolic rates for glucose, significant differences between these two populations can be demon-

strated. The same investigators have proposed adopting a similar approach for assessing global normal organ function and overall disease activity in other settings⁴⁷ This concept would require calculating tissue volume by utilizing modern computer based algorithms and accurate (partial volume corrected) measurement of metabolic activities (or other functional process) at each site of interest. As noted above, with recent advances made in such domains, it is feasible to correct for partial volume effects on low spatial resolution functional imaging techniques. By multiplying partial volume corrected metabolic measures (such as SUV, rates of metabolism, etc.) by volumetric measures from structural images to yield the MVP for the organ of interest or the diseased site, it would be feasible to calculate the global function in the intended tissues. By combining these measurements in the entire body for various pathological states, one can calculate the global metabolic activity of the underlying process. The power of this concept stems from its ability to rely on both structural and functional alterations that take place as a consequence of normal processes such as aging or disease states. This is important, as it is well documented that existing unidimensional measurement (Response Evaluation. Criteria in Solid Tumors, or RECIST) criteria, a standard ROI-based SUV, or other semiquantitative measurements are often prone to inaccuracy and high variability in their generated results.¹³

This concept is particularly applicable to cancer both at the initial stage and following treatment. The use of this approach may prove to be essential for testing new therapeutic agents. Similarly, this approach can be effectively employed in other states such as atherosclerosis, cardiac disorders, and central nervous system diseases. Below, we present some data generated based on these concepts.

Applications of Global Metabolic Activity in Neurology

One of the major domains of neurology in which the assessment of global metabolic activity is of great interest is that of neuropsychiatric disorders. To elucidate the relationship between reduced cognitive function and cerebral metabolism in patients with AD, Alavi and coworkers⁶³ hypothesized that the absolute amount of glucose used by the entire brain would prove to be a more reliable indicator of disease than metabolic rates calculated for a unit of brain weight alone.

Table 2 Whole Brain PET Data for AD and Controls⁶³

	CMRGlc (Uncorrected) (Mean ± SD)	CMRGlc (Corrected) (Mean ± SD)	Atrophy-Weighted Total Brain Metabolism (Mean ± SD)	Absolute Whole-Brain Metabolism (Mean ± SD)
AD patients	3.15 ± 0.83*	3.91 ± 1.02†	29.96 ± 7.90‡	37.24 ± 9.65§
Control patients	3.83 ± 0.70	4.43 ± 0.87	39.09 ± 7.02	45.09 ± 8.52

*Significantly different from controls, $P = 0.01$.

†Not significantly different from controls, $P = 0.11$.

‡Significantly different from controls, $P = 0.0008$.

§Significantly different from controls, $P = 0.014$.

They investigated 20 patients with the probable diagnosis of AD and 17 age-matched controls who underwent FDG-PET imaging and MR imaging within a few days of each other. The uncorrected cerebral metabolic rate for glucose (CMRGlc) values were atrophy-corrected using the following equation:

Atrophy corrected average CMRGlc

$$= \frac{\text{Mean CMRGlc}}{\text{Percentage of brain tissue in the intracranial volume}} \quad (5)$$

Absolute whole brain metabolism was calculated by using the formula:

Absolute whole brain metabolism

$$= \text{Atrophy corrected mean CMRGlc} \times \text{Brain volume} \quad (6)$$

Average metabolic rates, when corrected for atrophy, were 3.91 ± 1.02 and 4.43 ± 0.87 (mg of glucose per 100 cm³ brain tissue per minute) for AD patients and controls, respectively. Two other indices were determined as well: atrophy-weighted total brain metabolism (calculated by multiplying the brain volume, determined from MR image analysis, by the average metabolic rate) and absolute whole brain metabolism (calculated by multiplying the brain volume by the average metabolic rate corrected for atrophy). The former showed a very significant difference between the 2 groups (29.96 ± 7.90 for AD patients compared with 39.1 ± 7.0 for controls, $P < 0.001$). Atrophy-weighted total brain metabolism also correlated with mini-mental status examination scores ($r = 0.59$, $P < 0.01$). Absolute whole brain metabolism was found to be significantly different between AD and control groups and correlated well with mini-mental status examination scores. These data demonstrated that although

the metabolic rate per unit weight of the brain is unchanged in AD compared with controls, atrophy-weighted total brain metabolism and absolute whole brain metabolism are significantly affected. They concluded that both indices could prove to be sensitive correlates for cognitive dysfunction in AD (Tables 2 and 3).

Application of Global Metabolic Activity for Quantitation of Atherosclerosis

Bural and coworkers⁶⁴ described a technique for quantitating the extent of atherosclerosis in the aorta by multiplying SUVs in the aortic wall with aortic wall volumetric data provided by CT to yield MVPs. They examined this approach in 18 patients who had both FDG-PET and contrast-enhanced CT of the chest and abdomen. All had homogeneous diffuse FDG uptake in all segments of the aortic wall. The patients were divided into 3 groups according to their age, and FDG uptake was measured in different segments of the aorta by calculating the mean SUV for each segment. On each axial CT image, ROI tracings along the inner and outer wall contours of the aorta were generated. The inner surface area was subtracted from the outer surface area, and net area values for each segment were subsequently multiplied by slice thickness to calculate aortic wall volume. By multiplying SUV by the wall volume, they were able to calculate the atherosclerotic burden (AB; a special instance of the MVP) for each segment of the aorta. They then compared the aortic wall volumes, SUVs, and AB values in each arterial segment for each age group. When the aortic wall volumes, SUVs, and AB values in each aortic segment for each age group were compared, AB

Table 3 Recovered Whole Brain PET Data for AD and Controls⁶³

	Recovered CMRGlc (Uncorrected) (Mean ± SD)	CMRGlc (Corrected) (Mean ± SD)	Atrophy-Weighted Total Brain Metabolism (Mean ± SD)	Absolute Whole Brain Metabolism (Mean ± SD)
AD patients	4.89 ± 1.22*	6.06 ± 1.48†	46.61 ± 12.24‡	57.86 ± 14.89§
Control patients	5.38 ± 0.88	6.22 ± 1.07	55.23 ± 9.82	63.73 ± 10.07

CMRGlc in mg glucose/100 ml/brain tissue/min; atrophy-weighted total brain metabolism in mg glucose/brain/min; absolute whole brain metabolism in mg glucose/brain/min.

*Not significantly different from controls, $P = 0.17$.

†Not significantly different from controls, $P = 0.72$.

‡Significantly different from controls, $P = 0.026$.

§Significantly different from controls, $P = 0.18$.

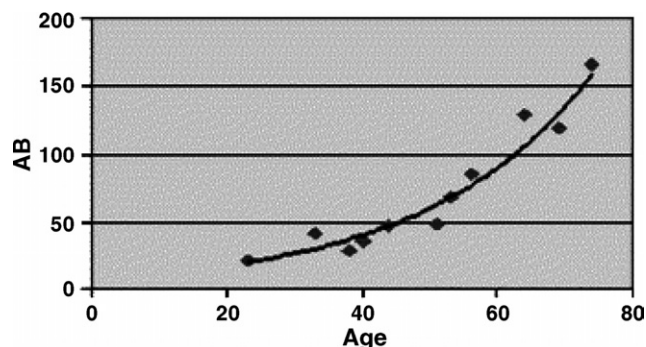


Figure 10 Assessment of changes in global metabolic activity of aortic atherosclerosis (atheroburden) with increasing age. (Reprinted with permission from Bural et al.⁶⁴)

values, SUVs, and wall volumes were found to increase with age ($P < 0.05$; Fig. 10 and Table 4).

Application of Global Metabolic Activity to Diffuse Hepatic Steatosis

Bural and coworkers⁴⁷ adopted this approach to compare the FDG uptake in liver and hepatic MVPs between normal subjects and subjects with diffuse hepatic steatosis by using FDG-PET and MR imaging. They investigated 24 subjects in this study (11 men, 13 women, age range 21-75 years). All subjects had FDG -PET and MR scans within a time interval of 52 ± 60 days. Twelve of the 24 subjects had the diffuse hepatic steatosis based on MR imaging criteria. The remaining 12 were selected as age-matched subjects, as they had normal appearing livers on MR images and on FDG-PET scans. They calculated the mean and maximum hepatic SUVs for both groups for every subject from the FDG-PET images. They also calculated the volume of the liver for each subject from MR images by summing the surface area values and multiplying by slice thickness. Subsequently, the hepatic MVP was calculated by multiplying liver volume by the mean hepatic SUV in each subject. The mean and maximum hepatic SUVs and the hepatic MVPs were compared for two groups. Mean and maximum hepatic SUVs for the group with diffuse hepatic steatosis were 2.2 ± 0.1 and 3.2 ± 0.4 , respectively, and 1.8 ± 0.2 and 2.4 ± 0.3 for the control group, respectively, which were all statistically significantly different ($P < 0.05$). Hepatic MVP for the group with diffuse hepatic steatosis was 3.7 ± 0.2 (SUV - L), and 2.3 ± 0.9 (SUV - L)

for the control group, which were statistically significantly different ($P < 0.05$).

Application of Global Metabolic Activity in Oncology

Investigators from the University of Pennsylvania have examined the concept of whole body metabolic burden (WBMB) in assessing disease activity in lymphoma patients.⁴⁷ Individual lesion metabolic burden (MB) was calculated by measuring the volume on CT (V_{CT}), the mean SUV measured on PET of the CT volume (SUV_{meanCT}), and the recovery coefficient (RC):

$$MB = SUV_{meanCT}(V_{CT})/RC \quad (7)$$

where RC recovers counts that extend beyond the CT volume as the result of partial volume effects and was obtained from a calibration plot study of hot sphere activity within a warm background phantom for the PET scanner used. For lesions >3 cm, RC was 1. The preliminary results showed that MB is a useful measure when corrected for partial volume effects and operator error in drawing ROIs. The WBMB was defined as the sum of the individual metabolic burden of all lesions identified. This index appeared promising to monitor changes in total body tumor burden in patients undergoing treatment.

$$WBMB = \sum_{i=1}^n MB_i \quad (8)$$

where n is the number of individual tumors outlined. Akin to single lesion MB, the WBMB had units of SUV - volume. Examples of this have been depicted in Table 5.

More recently, Larson and coworkers⁶⁵ proposed the concept of total lesion glycolysis (TLG), which was defined as $TLG = SUV_{mean} \times \text{volume of PET lesion}$. They further defined the response index (also known as Larson-Ginsberg Index, LGI) as:

$$\Delta TLG(LGI) = \frac{[(SUV_{mean})_1 \times (Vol)_1 - (SUV_{mean})_2 \times (Vol)_2]}{(SUV_{mean})_1 \times (Vol)_1} \times 100 \quad (9)$$

where "1" and "2" denote the pre- and post-treatment FDG-PET scans, respectively. They investigated a group of 41 locally advanced lung ($n = 2$), rectal ($n = 17$), esophageal ($n =$

Table 4 SUVs (Mean \pm SD) for Each Aortic Segment and for the Total Aorta⁶⁴

Age (Years)	Ascending Aorta	Arch of the Aorta	Descending Thoracic		Total SUV
			Aorta	Abdominal Aorta	
21-40 (n = 5)	1.7 \pm 0.3	1.8 \pm 0.3	1.7 \pm 0.3	1.6 \pm 0.3	1.7 \pm 0.3
41-60 (n = 7)	2.0 \pm 0.4	1.9 \pm 0.5	2.1 \pm 0.5	1.8 \pm 0.2	2.0 \pm 0.4
61-80 (n = 6)	2.3 \pm 0.3	2.3 \pm 0.1	2.4 \pm 0.3	2.2 \pm 0.4	2.3 \pm 0.3
P value	0.04	0.07	0.03	0.04	0.001

Table 5 Pre- and Post-treatment Assessment of Global Metabolic Burden (Volume \times SUV) in Patients With Lymphoma

Case #	Pre-Treat			Post-Treat			Pre-Treat			Post-Treat		
	SUV _{mean}	SUV _{mean}	% Change	SUV _{max}	SUV _{max}	% Change	Tumor Volume	Tumor Volume	% Change	MB	MB	% Change
1	3.4	0	100	11.3	0	100	58	5	91	199	0	100
2	2.3	0.8	67	6.3	2	69	152	34	78	333	78	77
3	17	12	29	23	12.5	24	50	50	0	850	600	29

16) and gastric (n = 6) cancers. They concluded that the visual response score and Δ TLG are substantially correlated with other response parameters and are highly reproducible.

Future Applications and Advances for Quantitative Imaging Techniques

The role of PET during the past decade has evolved rapidly from that of a pure research tool to a methodology of enormous importance in specialties such as oncology. FDG-PET is widely used for the diagnosis, staging, assessment of tumor response to therapy, and detection of tumor recurrence because metabolic changes usually precede changes that are associated with structural imaging alone including tumor size.

During the next few years, it is expected that sophisticated quantitative analysis methodologies will become widely available in clinical settings and will not be limited to research in PET facilities with advanced scientific and technical support. As a result, it is likely that commercial software for accurate quantitative analysis will undergo major adjustments in the future to meet the challenges that will be faced in the routine and practical applications of this approach.

References

- Alavi A, Reivich M, Greenberg J, et al: Mapping of functional activity in brain with 18F-fluoro-deoxyglucose. *Semin Nucl Med* 11:24-31, 1981
- Reivich M, Alavi A, Wolf A, et al: Use of 2-deoxy-D[1-11C]glucose for the determination of local cerebral glucose metabolism in humans: Variation within and between subjects. *J Cereb Blood Flow Metab* 2:307-319, 1982
- Zaidi H (ed): *Quantitative Analysis in Nuclear Medicine Imaging*. New York, Springer, 2006
- Carson R: Tracer kinetic modeling in PET, in Valk PE, Bailey DL, Townsend DW, et al (eds): *Positron Emission Tomography: Basic Science and Clinical Practice*. Chapter 4 ed. London, Springer-Verlag, 2003, pp 147-179
- Sokoloff L, Reivich M, Kennedy C, et al: The [¹⁴C]deoxyglucose method for the measurement of local cerebral glucose utilization: Theory, procedure, and normal values in the conscious and anesthetized albino rat. *J Neurochem* 28:897-916, 1977
- Reivich M, Kuhl D, Wolf A, et al: The [18F]fluorodeoxyglucose method for the measurement of local cerebral glucose utilization in man. *Circ Res* 44:127-137, 1979
- Phelps ME, Huang SC, Hoffman EJ, et al: Tomographic measurement of local cerebral glucose metabolic rate in humans with (F-18)2-fluoro-2-deoxy-D-glucose: Validation of method. *Ann Neurol* 6:371-388, 1979
- Gjedde A: Calculation of cerebral glucose phosphorylation from brain uptake of glucose analogs in vivo: A re-examination. *Brain Res Rev* 4:237-274, 1982
- Patlak CS, Blasberg RG, Fenstermacher JD: Graphical evaluation of blood-to-brain transfer constants from multiple-time uptake data. *J Cereb Blood Flow Metab* 3:1-7, 1983
- Huang S-C: Anatomy of SUV. *Nucl Med Biol* 27:643-646, 2000
- Minn H, Leskinen-Kallio S, Lindholm P, et al: [18F]fluorodeoxyglucose uptake in tumors: Kinetic vs. steady-state methods with reference to plasma insulin. *J Comput Assist Tomogr* 17:115-123, 1993
- Kole A, Nieweg O, Pruijm J, et al: Standardized uptake value and quantification of metabolism for breast cancer imaging with FDG and L-[1-11C]tyrosine PET. *J Nuc Med* 38:692-696, 1997
- Keyes J: SUV: Standard uptake value or silly useless value? *J Nucl Med* 36:1836-1839, 1995

14. Kim CK, Gupta N, Chandramouli B, et al: Standardized uptake values of FDG: Body surface area correction is preferable to body weight correction. *J Nucl Med* 35:164-167, 1994
15. Kim CK, Gupta N: Dependency of standardized uptake values of fluorine-18 fluorodeoxyglucose on body size: Comparison of body surface area correction and lean body mass correction. *Nucl Med Commun* 17:890-894, 1996
16. Gupta N, Frank A, Dewan N, et al: Solitary pulmonary nodules: Detection of malignancy with PET with 2-[F-18]-fluoro-2-deoxy-D-glucose. *Radiology* 184:441-444, 1992
17. Zasadny KR, Wahl RL: Standardized uptake values of normal tissues at PET with 2-[fluorine-18]-fluoro-2-deoxy-D-glucose: Variations with body weight and a method for correction. *Radiology* 189:847-850, 1993
18. Avril N, Bense S, Ziegler SI, et al: Breast imaging with fluorine-18-FDG PET: Quantitative image analysis. *J Nucl Med* 38:1186-1191, 1997
19. Zhuang HM, Cortes-Blanco A, Pourdehnad M, et al: Do high glucose levels have differential effect on FDG uptake in inflammatory and malignant disorders? *Nucl Med Commun* 22:1123-1128, 2001
20. Hamberg LM, Hunter GJ, Alpert NM, et al: The dose uptake ratio as an index of glucose metabolism: Useful parameter or oversimplification? *J Nucl Med* 35:1308-1312, 1994
21. Kung JW, Yu JQ, Evans T, et al: FDG uptake at extended time periods in non small cell cancer—Implications for improved cancer management. Proceedings of 51st Annual Meeting of Society of Nuclear Medicine. *J Nucl Med* 19-23, 2004
22. Hustinx R, Smith RJ, Benard F, et al: Dual time point fluorine-18 fluorodeoxyglucose positron emission tomography: A potential method to differentiate malignancy from inflammation and normal tissue in the head and neck. *Eur J Nucl Med* 26:1345-1348, 1999
23. Matthies A, Hickeson M, Cuchiara A, et al: Dual time point 18F-FDG PET for the evaluation of pulmonary nodules. *J Nucl Med* 43:871-875, 2002
24. Boerner AR, Weckesser M, Herzog H, et al: Optimal scan time for fluorine-18 fluorodeoxyglucose positron emission tomography in breast cancer. *Eur J Nucl Med* 26:226-230, 1999
25. Kumar R, Loving VA, Chauhan A, et al: Potential of dual-time-point imaging to improve breast cancer diagnosis with 18F-FDG PET. *J Nucl Med* 46:1819-1824, 2005
26. Mavi A, Urhan M, Yu JQ, et al: Dual time point 18F-FDG PET imaging detects breast cancer with high sensitivity and correlates well with histologic subtypes. *J Nucl Med* 47:1440-1446, 2006
27. Nishiyama Y, Yamamoto Y, Fukunaga K, et al: Dual-time-point 18F-FDG PET for the evaluation of gallbladder carcinoma. *J Nucl Med* 47:633-638, 2006
28. Ma SY, See LC, Lai CH, et al: Delayed (18)F-FDG PET for detection of paraaortic lymph node metastases in cervical cancer patients. *J Nucl Med* 44:1775-1183, 2003
29. Spence AM, Muzi M, Mankoff DA, et al: 18F-FDG PET of gliomas at delayed intervals: Improved distinction between tumor and normal gray matter. *J Nucl Med* 45:1653-1659, 2004
30. Zhuang H, Pourdehnad M, Lambright ES, et al: Dual time point 18F-FDG PET imaging for differentiating malignant from inflammatory processes. *J Nucl Med* 42:1412-1417, 2001
31. Houseni M, Chamroonrat W, Bural G, et al: Promising role of dual time FDG-PET imaging in assessing focal and diffuse bone marrow disorders. *J NUCL Med* 47:227P, 2006
32. Chawluk J, Alavi A, R D, et al: Positron emission tomography in aging and dementia: Effect of cerebral atrophy. *J Nucl Med* 28:431-437, 1987
33. Tanna NK, Kohn MI, Horwich DN, et al: Analysis of brain and cerebrospinal fluid volumes with MR imaging: Impact on PET data correction for atrophy. Part II: Aging and Alzheimer dementia. *Radiology* 178: 123-130, 1991
34. Rousset OG, Ma Y, Evans AC: Correction for partial volume effects in PET: Principle and validation. *J Nucl Med* 39:904-911, 1998
35. Aston JA, Cunningham VJ, Asselin MC, et al: Positron emission tomography partial volume correction: estimation and algorithms. *J Cereb Blood Flow Metab* 22:1019-1034, 2002
36. Quarantelli M, Berkouk K, Prinster A, et al: Integrated software for the analysis of brain PET/SPECT studies with partial-volume-effect correction. *J Nucl Med* 45:192-201, 2004
37. Baete K, Nuyts J, Laere KV, et al: Evaluation of anatomy based reconstruction for partial volume correction in brain FDG-PET. *NeuroImage* 23:305-317, 2004
38. Giovacchini G, Toczek MT, Bonwetsch R, et al: 5-HT1A receptors are reduced in temporal lobe epilepsy after partial-volume correction. *J Nucl Med* 46:1128-1135, 2005
39. Zaidi H, Ruest T, Schoenahl F, et al: Comparative evaluation of statistical brain MR image segmentation algorithms and their impact on partial volume effect correction in PET. *Neuroimage* 32:1591-1607, 2006
40. Weber W, Young C, Abdel-Dayem HM, et al: Assessment of pulmonary lesions with 18F-fluorodeoxyglucose positron imaging using coincidence mode gamma cameras. *J Nucl Med* 40:574-578, 1999
41. Hickeson M, Yun M, Matthies A, et al: Use of a corrected standardized uptake value based on the lesion size on CT permits accurate characterization of lung nodules on FDG-PET. *Eur J Nucl Med Mol Imaging* 29:1639-1647, 2002
42. Lubberink M, Tolmachev V, Widstrom C, et al: 110mIn-DTPA-D-Phe1-octreotide for imaging of neuroendocrine tumors with PET. *J Nucl Med* 43:1391-1397, 2002
43. Muller-Gartner HW, Links JM, Prince JL, et al: Measurement of radio-tracer concentration in brain gray matter using positron emission tomography: MRI-based correction for partial volume effects. *J Cereb Blood Flow Metab* 12:571-583, 1992
44. Meltzer CC, Zubieta JK, Links JM, et al: MR-based correction of brain PET measurements for heterogeneous gray matter radioactivity distribution. *J Cereb Blood Flow Metab* 16:650-658, 1996
45. Kohn MI, Tanna NK, Herman GT, et al: Analysis of brain and cerebrospinal fluid volumes with MR imaging. Part I. Methods, reliability, and validation. *Radiology* 178:115-122, 1991
46. Zhuge Y, Liu J, Udupa JK: Membership-based multiprotocol MR brain image segmentation, in: Sonka M, Fitzpatrick JM (eds): *Medical Imaging 2003: Image Processing*. Vol 5032. San Diego, CA, SPIE, 2003, 1572-1579
47. Bural G, Zhuge Y, Torigian D, et al: Partial volume correction and segmentation allows accurate measurement of SUV for the grey matter in the brain. *J NUCL Med* 47:9P, 2006
48. Zaidi H: Medical image segmentation: Quo Vadis. *Comput Meth Prog Biomed* 84:63-67, 2006
49. Bezdek JC, Hall LO, Clarke LP: Review of MR image segmentation techniques using pattern recognition. *Med Phys* 20:1033-1048, 1993
50. Duncan JS, Ayache N: Medical image analysis: Progress over two decades and the challenges ahead. *IEEE Trans Patt Anal Mach Intell* 22:85-106, 2000
51. Olabarriaga SD, Smeulders AW: Interaction in the segmentation of medical images: A survey. *Med Image Anal* 5:127-142, 2001
52. Montgomery DWG, Amira A, Zaidi H: Fully automated segmentation of oncological PET volumes using a combined multiscale and statistical model. *Med Phys* 34:722-736, 2007
53. Behloul F, Lelieveldt BP, Boudraa A, et al: Neuro-fuzzy systems for computer-aided myocardial viability assessment. *IEEE Trans Med Imaging* 20:1302-1313, 2001
54. Wong K-P, Dagan F, Meikle SR, et al: Segmentation of dynamic PET images using cluster analysis. *IEEE Trans Nucl Sci* 49:200-207, 2002
55. Boudraa A, Cexus J-C, Zaidi H: Functional segmentation of dynamic nuclear medicine images by cross-PsiB energy operator. *Comput Meth Prog Biomed* 84:148-154, 2006
56. Zaidi H, Hasegawa BH: Determination of the attenuation map in emission tomography. *J Nucl Med* 44:291-315, 2003
57. Zaidi H, Xu XG: Computational anthropomorphic models of the human anatomy: The path to realistic Monte Carlo modeling in radiological sciences. *Annu Rev Biomed Eng* 2007 Feb 13 [Epub ahead of print]
58. Udupa JK, Odhner D, Samarasekera S, et al: 3DVIEWNIX: an open, transportable, multidimensional, multimodality, multiparametric imaging software system, in: Kim Y (ed): *Medical Imaging 1994: Image Capture, Formatting, and Display*. Vol 2164. Newport Beach, CA, SPIE, 1994, pp 58-73
59. Paulino AC, Thorstad WL, Fox T: Role of fusion in radiotherapy treatment planning. *Semin Nucl Med* 33:238-243, 2003
60. Thireou T, Kontaxakis G, Strauss LG, et al: Feasibility study of the use of similarity maps in the evaluation of oncological dynamic

- positron emission tomography images. *Med Biol Eng Comput* 43:23-32, 2005
61. Frouin V, Comtat C, Reilhac A, et al: Correction of partial volume effect for PET striatal imaging: fast implementation and study of robustness. *J Nucl Med* 43:1715-1726, 2002
 62. Zaidi H, Montandon M-L, Slosman DO: Magnetic resonance imaging-guided attenuation and scatter corrections in three-dimensional brain positron emission tomography. *Med Phys* 30:937-948, 2003
 63. Alavi A, Newberg AB, Souder E, et al: Quantitative analysis of PET and MRI data in normal aging and Alzheimer's disease: Atrophy weighted total brain metabolism and absolute whole brain metabolism as reliable discriminators. *J Nucl Med* 34:1681-1687, 1993
 64. Bural GG, Torigian DA, Chamroonrat W, et al: Quantitative assessment of the atherosclerotic burden of the aorta by combined FDG-PET and CT image analysis: A new concept. *Nucl Med Biol* 33:1037-1043, 2006
 65. Larson SM, Erdi Y, Akhurst T, et al: Tumor treatment response based on visual and quantitative changes in global tumor glycolysis using PET-FDG imaging. The visual response score and the change in total lesion glycolysis. *Clin Positron Imaging* 2:159-171, 1999